nature portfolio

https://doi.org/10.1038/s41567-022-01639-3

Supplementary information

Size-controlled quantum dots reveal the impact of intraband transitions on high-order harmonic generation in solids

In the format provided by the authors and unedited

Supplementary Information for

Size-controlled quantum dots reveal the impact of intraband transitions on high-order harmonic generation in solids

Kotaro Nakagawa[1], Hideki Hirori[1], Shunsuke A. Sato[2,3], Hirokazu Tahara[1], Fumiya Sekiguchi[1], Go Yumoto[1], Masaki Saruyama[1], Ryota Sato[1], Toshiharu Teranishi[1], and Yoshihiko Kanemitsu[1]

[1]*Institute for Chemical Research, Kyoto University, Uji, Kyoto 611-0011, Japan*

[2]*Center for Computational Sciences, University of Tsukuba, Tsukuba 305-8577, Japan*

[3]*Max Planck Institute for the Structure and Dynamics of Matter, Luruper Chaussee 149, 22761 Hamburg, Germany*

I. Quantum dot (QD) synthesis

A. Chemicals

We used the following chemicals as received without further purification: Se (99.99%, Aldrich), 1-octadecene (ODE, 90%, Aldrich), CuCl (95+%, Wako), oleylamine (80–90%, Acros), oleic acid (TCI), Cd acetate dihydrate (98+%, Wako), dibenzyl ether (97+%, Wako), tri-*n*-octylphosphine (TOP, 97%, Aldrich), CdO (99.99%, Aldrich), myristic acid (99%, TCI), Cd stearate (98%, Angene), stearic acid (95+%, Wako), and tri-*n*-octylphosphine oxide (TOPO, 90%, Aldrich).

B. Large CdSe QDs (14 nm)

The zincblende CdSe QDs with an average diameter of about 14 nm were synthesized by a cation exchange reaction using berzelianite $Cu_{2-x}Se$ QDs.

Synthesis of $Cu_{2-x}Se$ QDs (Ref. [1]):

First, Se (2 mmol) was dissolved in ODE (20 mL) at 250 °C under an N_2 atmosphere. Then, CuCl (2 mmol), oleylamine (12 mmol), and oleic acid (4 mmol) were added to the Se–ODE solution at room temperature, and the mixture was kept at 200 °C for 15 min under the N_2 atmosphere. The synthesized $Cu_{2-x}Se$ QDs were collected by adding ethanol and subsequent centrifugation. Then, they were redispersed in hexane for the following cation exchange reaction.

Cation exchange with Cd^{2+} ions (Ref. [2]):

A Cd^{2+} solution was prepared by heating a mixture of Cd acetate (1.1 mmol), oleylamine (8 mL), ODE (2 mL), and dibenzyl ether (15 mL) at 110 °C under an N_2 atmosphere. A solution of the $Cu_{2-x}Se$ QDs (containing 0.2 mmol Cu) dispersed in TOP (2 mL) was injected into the Cd^{2+} solution at 50 °C, and the mixture was kept at 110 °C for 20 min under the N_2 atmosphere. The synthesized CdSe QDs were purified in a two-step process using 2-propanol, and then redispersed in hexane for further use.

C. Small CdSe QDs (1.8–6.4 nm)

Synthesis of the 6.4-nm-large CdSe QDs (Ref. [3]):

First, a mixture of CdO (1 mmol), myristic acid (2.2 mmol), and ODE (4 mL) was heated to 290 °C under an N_2 atmosphere until the solution turned colorless to form Cd-myristate complexes. A suspension consisting of Se (0.05 mmol) and ODE (1 mL) was injected into the Cd-myristate solution at 250 °C, and kept at that temperature for 10 min. Then, oleic acid (0.5 mL) was added dropwise, which was followed by injecting a suspension consisting of Se (0.05 mmol) and ODE (0.5 mL) dropwise and keeping the solution at 250 °C for further 10 min. The obtained turbid solution (6 mL) was mixed with acetone (6 mL) and centrifuged, and the supernatant was removed. The precipitate was mixed with a toluene solution (3.3 mL) containing 10 vol% oleic acid, and heated at 100 °C on a hotplate until it turned transparent. The QDs were collected by adding methanol (3 mL) and centrifugation. Then, this ligand exchange process with oleic acid was repeated, and the obtained QDs were redispersed in hexane for further use.

Synthesis of the 4.5-nm-, 3.8-nm-, and 3.1-nm-large CdSe QDs (Ref. [3]):

First, a mixture of Cd stearate (0.2 mmol), stearic acid (0.4 mmol), and ODE (6 mL) was heated to 250 °C under an N_2 atmosphere. A suspension consisting of Se (0.04 mmol) and ODE (0.8 mL) was injected to the Cd-stearate solution at 250 °C, and the mixture was kept at that temperature for 5 or 10 min under the N_2 atmosphere to obtain 3.1-nm- or 3.8-nm-large CdSe QDs, respectively. For further growth, the additional suspension containing Se (0.15 mmol) and ODE (3.0 mL) was added dropwise at 1.0 mL/h to reach 4.5 nm. The product was purified using the same procedure as for the 6.4-nm-large CdSe QDs. The QDs were redispersed in hexane for further use.

Syntheses of the 2.8-nm-, 2.4-nm-, and 2.1-nm-large CdSe QDs (Ref. [4]):

First, a mixture of CdO (0.2 mmol), oleic acid (0.8 mmol), and ODE (6.3 mL) was heated to 250 °C under an N_2 atmosphere until the solution turned colorless to form Cd-oleate complexes. After the solution cooled to room temperature, oleylamine (5.6 mmol) and TOPO (1.3 mmol) were added to the Cd-oleate solution, and the mixture was heated to 270 °C under the N_2 atmosphere to synthesize CdSe QDs with an average diameter of about 2.8 nm. In the case of preparing the 2.4-nm- and 2.1-nm-large CdSe QDs, we

used lower temperatures in the last step (240 °C and 200 °C, respectively). Immediately after the injection of a Se (1.5 mmol)–TOP (1 mL) solution into the Cd-oleate solution, the heater was removed to quench the reaction. The synthesized CdSe QDs were purified with ethanol, and redispersed in hexane for further use.

Synthesis of 1.8-nm-large CdSe QDs (Ref. [3]):

First, a mixture of Cd stearate (0.2 mmol), stearic acid (0.4 mmol), and ODE (6 mL) was heated to 200 °C under an N_2 atmosphere. A suspension consisting of Se (0.04 mmol) and ODE (0.8 mL) was injected to the Cd-stearate solution at 200 °C. The heater was removed immediately after the Se–ODE injection. The product was purified by the same procedure as used for the 6.4-nm-large CdSe QDs. The QDs were redispersed in hexane for further use.

D. Small CdS QDs (1.6–3.5 nm)

Syntheses of 3.5-nm-, 2.9-nm-, 2.4-nm-, 2.1-nm-, and 1.6-nm-large CdS QDs (Ref. [5]):

First, a mixture of CdO (0.6 mmol), oleic acid (3.6 mL), and ODE (24 mL) was heated at 240 °C under an N_2 atmosphere until the solution turned colorless to form Cd-oleate complexes. An S–ODE solution was prepared separately by dissolving S (0.625 mmol) in ODE (10 mL) at 200 °C under an N_2 atmosphere. The S–ODE solution was rapidly injected into the Cd-oleate solution. The size of the CdS QDs was controlled by adjusting the solution temperature during the S–ODE injection and the subsequent holding time as follows: 3.5 nm (240 °C, 90 s), 2.9 nm (240 °C, 75 s), 2.4 nm (190 °C, 1 h), 2.1 nm (140 °C, 3 h), and 1.6 nm (90 °C, 1 h). The synthesized CdS QDs were purified with acetone, and redispersed in hexane for further use.

E. Characterization of QDs

Transmission electron microscopy (TEM) images were obtained using an accelerating voltage of 120 kV (HT7820, HITACHI). The average sizes of the QDs were estimated by measuring the diameters of 200 particles in the TEM images. X-ray diffraction (XRD) measurements were conducted using a diffractometer with CuKα radiation operated at 45 kV and 40 mA (X'Pert Pro MPD, Panalytical). We confirmed that QDs used here have a zincblende crystal structure.

F. Optical absorption spectra of CdSe and CdS QDs

The optical absorption spectra of the synthesized samples in the visible region are shown in Fig. S1. We plot the optical density (OD) versus the photon energy.

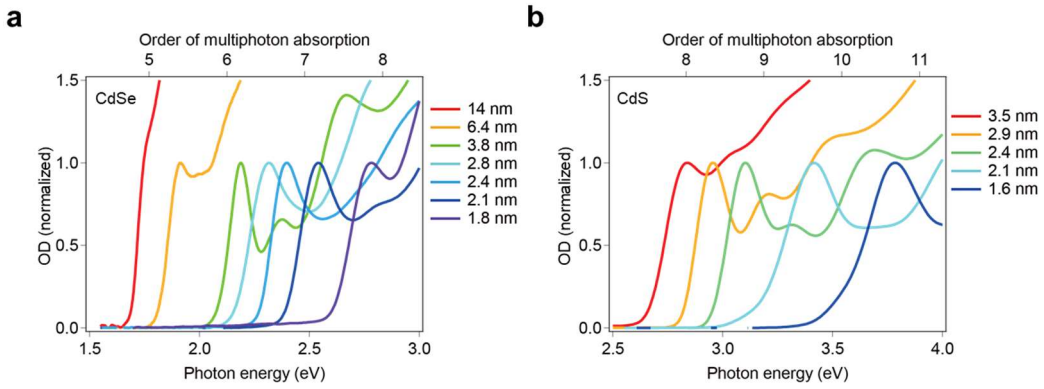

Fig. S1. Absorption spectra of (a) CdSe and (b) CdS QDs. The upper axis indicates the photon energy in terms of 0.35-eV photons, and thus the upper axis provides the number of photons required to excite a carrier to a given energy level in a multiphoton absorption process. The ODs are normalized by the lowest energy exciton peaks.

II. Excitation intensity dependence of HHG

Figure S2 shows the excitation intensity dependence of I_7 for six different CdSe QD films. The dashed lines are the fits of the data in the high-excitation regime (excitation intensity $I_{exc} > 0.35$ TW/cm^2) to the scaling law $I_{exc}{}^p$. In the high-excitation regime, the slopes of the intensity dependence become smaller. Furthermore, the scaling coefficients p are smaller than those predicted by perturbation theory, i.e., $p < 7$. This indicates that the high-order hamonic generation (HHG) mechanism in CdSe QDs under these excitation conditions is non-perturbative.

The general behaviour of the intensity-dependent slope p can be explained by the Keldysh parameter $\gamma = \omega(2mE_g)^{1/2}/eE$, where m is the effective electron mass, ω is the light frequency, E is the electric field amplitude, and E_g is the bandgap energy [6]. As γ decreases, the excitation process shifts from a multi-photon excitation process to a tunneling process, resulting in a non-perturbative behaviour. In our experiments, we observed that the value of p decreases as the QD size increases from 2.1 to 14 nm. This means that, as the size increases, the process becomes more non-perturbative, in other words, γ becomes smaller. Considering the factors included in the Keldysh parameter, this decrease in γ is attributed to the fact that the bandgap energy decreases from 2.6 to 1.8 eV as the QD size increases from 2.1 to 14 nm. In addition, if electrons in the conduction band of a bulk crystal are accelerated by an optical electric field, they pass through a continuum of states in momentum space, which corresponds to an intraband transition. In a structure with discrete electronic states due to quantum confinement, intraband transitions are less likely to occur due to energy gaps between the states. This means that electron acceleration is limited in real space, and it can be inferred that the effective mass in smaller QDs becomes larger. This increase of the effective mass could also explain the above-mentioned size dependence of the Keldysh parameter.

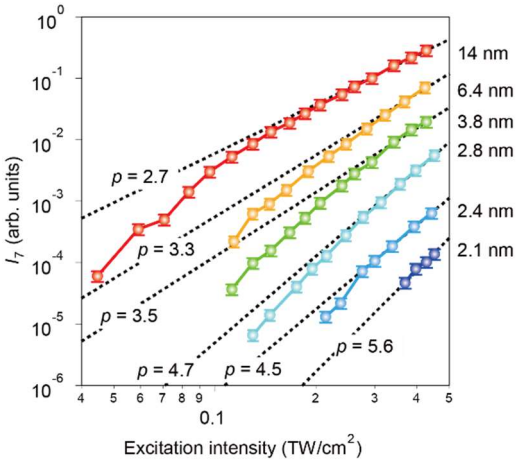

Fig. S2. The solid circles show I_7 as a function of I_{exc} for different QD diameters. The dashed lines are proportional to $I_{exc}{}^p$, where the values of p are obtained by fitting the data above 0.35 TW/cm^2 to $I_{exc}{}^p$. The data are offset for clarity.

III. Mid-infrared (MIR) pulse excitation induces no sample damage

Figure S3 shows the absorption spectra measured at the MIR excitation spot before and after the measurement of the HH spectra for CdSe and CdS QD films with small QD diameters (2.1 nm and 1.6 nm, respectively). The absorption was measured at the same position as that of the MIR-pulse excitation spot in order to verify whether sample damage occurred due to the MIR pulse or not. It can be verified that the linear absorption at the excitation spot did not change due to the MIR irradiation. Therefore, we infer that the observed small high-order harmonic (HH) intensities of QDs with average diameters below 3 nm was not due to sample damage.

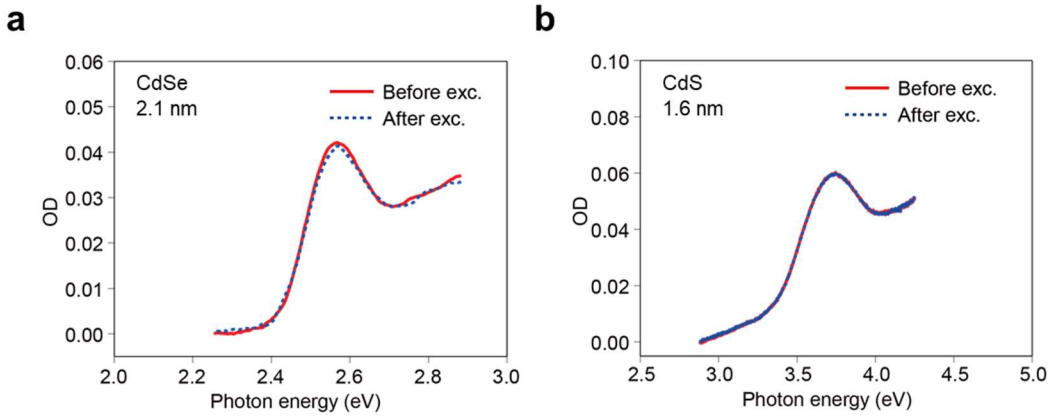

Fig. S3. Absorption spectra measured before (solid curve) and after (broken curve) the measurement of the HH spectra of CdSe and CdS QD films with average QD diameters of 2.1 nm and 1.6 nm, respectively.

IV. QD size dependence of HHG obtained using a different excitation wavelength

In order to avoid the additional small thermal-decay contribution in the TA signal that can appear if the ligands of the QDs absorb MIR light, it is necessary to use an excitation wavelength that is shorter than that used in the HH spectrum measurements shown in Fig. 1 in the main text. Therefore, we also verified that the different MIR excitation wavelength does not cause a significant change in the size dependence of the HHs as shown in Fig. S4.

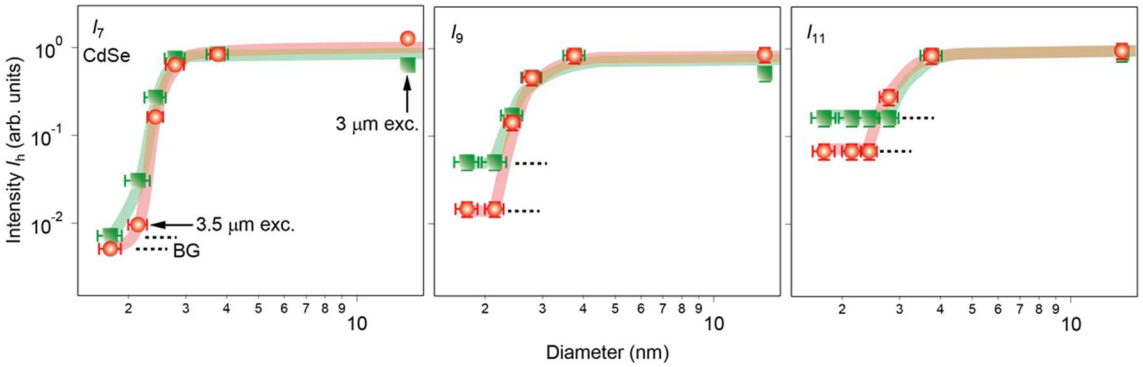

Fig. S4. Size dependence of I_7, I_9, and I_{11} 1for different excitation wavelengths. The green and the orange data were obtained using excitation wavelengths of 3 μm and 3.5 μm, respectively.

V. Estimation of the carrier density

Transient absorption (TA) measurements using visible and MIR pump pulses were performed to accurately determine the average number of excited carriers per QD. We measured four CdSe QD thin films prepared by drop-casting QDs with different sizes. We used QDs with d = 2.4, 2.8, 3.1, 3.8, 4.5, and 6.4 nm, and the band-edge exciton energies were 2.40, 2.31, 2.24, 2.19, and 1.91 eV, respectively.

An ytterbium-doped potassium gadolinium tungstate (Yb:KGW) based femtosecond laser system (Pharos, Light Conversion) was used as the light source. This system provided pulses with a center wavelength of 1033 nm and a pulse duration of 180 fs at a repetition rate of 1 kHz. The MIR pump pulses with a wavelength of 3 μm were generated by a homemade optical parametric amplifier, which was pumped by the fundamental 1033-nm pulses [7]. For the probe pulses, white light was generated by focusing the fundamental pulses into a 10-mm-thick quartz cell containing distilled water. The probe light transmitted through the sample was spectrally resolved by a spectrometer (SpectraPro 500i, Roper Scientific) and detected using a charge coupled device (CCD) camera (PIXIS-100F, Roper Scientific). To obtain a high signal-to-noise ratio, we synchronously chopped the pump beam at 500 Hz, measured the probe-pulse transmission spectra at 1 kHz, and evaluated the difference between the spectra with and without the pump beam.

Figure 3 in the main text shows the TA dynamics of CdSe QD thin films with different particle sizes in the case of MIR-pump TA measurements. Here, the excitation intensity was set to 0.36 TW/cm^2 and the probe wavelength was set to the energy of the band-edge excitons. We confirmed a decrease in photoabsorption after excitation with the pump pulse. This so-called photobleaching was caused by the excited electrons that occupy the band edge. In order to obtain the average number of excited carriers per QD from the differential transmission $\Delta T/T$, it is necessary to clarify the dependence of $\Delta T/T$ on the average number of excited excitons $\langle N \rangle$ per QD. Since visible pump–probe TA measurements are a standard method for determining the number of excited carriers, we also performed such measurements as explained below.

For the visible pump light, the second harmonic of the fundamental 1033-nm pulse was generated by using a beta barium borate (β-BBO) crystal. The probe pulses were generated and detected in the same way as explained above. The TA signals for different pump intensities were measured as shown in Fig. S5a. The increase in the photobleach signal with the excitation intensity indicates an increase in the number of excited carriers per QD. Under strong excitation conditions, a fast decay due to multiexcitons is observed within the first 100 ps, and this is followed by a relatively slow decay attributed to single excitons. To calculate

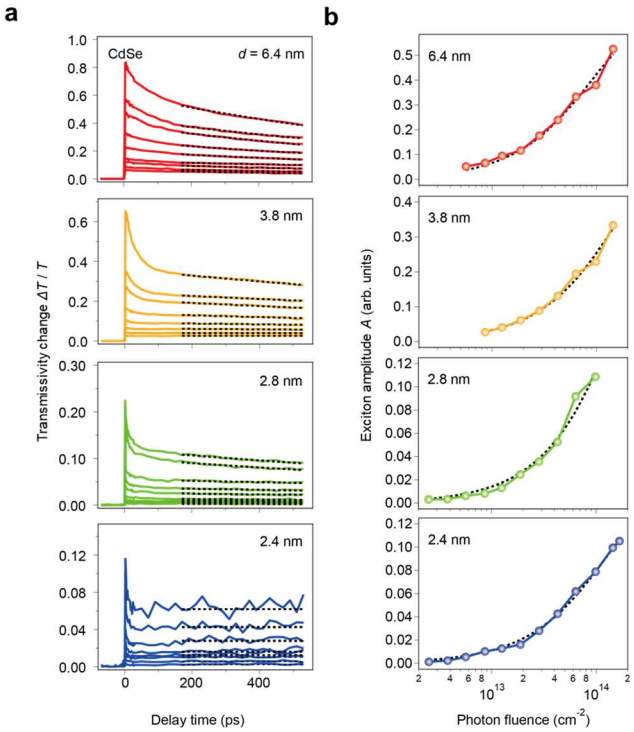

Fig. S5. a, The TA signals $\Delta T/T$ of CdSe QDs obtained in the TA measurements with the visible pump pulse. The black dashed curves are fits to an exponential function. **b,** The pump power dependence of the amplitude of single-exciton component. The dashed curves are the result of fitting the data points to the equation based on the Poisson distribution.

the carrier density, we use the single-exciton component observed after 150 ps. The amplitudes of the single-exciton component were obtained by fits of the TA signals in the range from 150 to 550 ps to an exponential decay function as shown by the dashed black curves in Fig. S5a, and are shown in Fig. S5b as a function of the excitation power (see the coloured circles).

This excitation power dependence can be explained by the absorption probability of photons. For this, we assume the Poisson distribution P_i (<*N*>), which is defined by $\langle N\rangle^i e^{-\langle N\rangle}/\ i!$ and describes the probability that *i* photons are absorbed by a QD when the average number of absorbed photons is <*N*>. The absorption of one or more photons is required to generate one or more excitons, and the generation of multiexcitons is followed by relaxation processes toward a single-exciton state. Thus, the probability of generating a single exciton after the relaxation is expressed by $\sum_{i\geq 1} P_i(\langle N\rangle)$, and we relate the TA signal and <*N*> as follows [8,9]: $\Delta T/T(\langle N\rangle) \propto \sum_{i\geq 1} P_i(\langle N\rangle) = 1 - e^{-\langle N\rangle}$. Here, the average number of excited excitons <*N*> can also be expressed by the product of the absorption cross section σ and the excitation photon density *J*, $\langle N\rangle = \sigma J$. The dashed curves in Fig. S5b are the result of fitting the excitation power dependence of the extracted amplitudes to the equation derived using the Poisson distribution. Since the relation between $\Delta T/T$ and <*N*> is independent of the pump wavelength, we can evaluate <*N*> from the MIR-pump TA data by using this relation (see the data points in Fig. 3c). The average number of excited carriers <*N*> per QD was determined to be 0.0061, 0.013, 0.22, and 1.4 for QDs with d = 2.4, 2.8, 3.8, and 6.4 nm, respectively. The corresponding values of the carrier density $n_d = \langle N\rangle/V$ are 0.43×10^{18}, 0.62×10^{18}, 4.1×10^{18}, and 5.3×10^{18} cm^{-3}, which is consistent with the size dependence of the HH intensity shown in Fig. 2 in the main text.

VI. Theoretical description of HHG

A. The one-dimensional dimer chain model

To discuss the effect of quantum confinement on HHG, we use a simple one-dimensional dimer chain model and calculate the light-induced electron dynamics. The system is described by the following Hamiltonian:

$$\hat{H}_0 = \sum_{j=1}^{2N+1} \left[-t_H \left(\hat{c}_{j+1}^{\dagger} \hat{c}_j + \hat{c}_{j-1}^{\dagger} \hat{c}_j \right) - \frac{(-1)^j}{2} \Delta \hat{c}_j^{\dagger} \hat{c}_j \right]. \quad (S2.1)$$

Here, we use the index j to label the sites of the chain where $1 \leq j \leq 2N+1$, and $\hat{c}_j^{\dagger}$ and $\hat{c}_j$ are the creation and annihilation operators for the jth site, respectively. For $j = 0$ and $j = 2N+2$, we assume $\hat{c}_j^{\dagger} = \hat{c}_j = 0$ (isolated boundary condition). The nearest neighbor hopping parameter is given by t_H, and the onsite energy gap (potential difference between the even site and the odd site) is given by $\Delta > 0$. The Hamiltonian can be diagonalized as shown below:

$$\hat{H}_0 = \sum_{n=1}^{2N+1} \epsilon_n \hat{a}_n^{\dagger} \hat{a}_n \,, \quad (S2.2)$$

where ϵ_n is the nth eigenenergy, and $\hat{a}_n^{\dagger}$ and $\hat{a}_n$ are creation and annihilation operators for the nth eigenstate. Here, we assume that the eigenenergies are arranged in increasing order, $\epsilon_{n+1} \geq \epsilon_n$. Note that the eigenenergies of the system can be classified into two energy bands: One band consists of N lower energy states, while the other band consists of $N+1$ higher energy states (Fig. S6). In the bulk limit ($N \to \infty$), the lower energy band corresponds to the valence band while the higher energy band corresponds to the conduction band. In the bulk limit with periodic boundary conditions, a direct-gap structure is obtained. Figure S6 shows an example of the band dispersion of the model with periodic boundary conditions by setting Δ equal to t_H. The valence and conduction bands can be clearly identified. In the bulk limit, the bandgap energy is given by $E_g = \Delta$, and the reduced electron–hole mass is given by $m^* = \Delta/(4t_H^2 a_L^2)$, where a_L denotes the lattice constant. In terms of the eigenenergies, the bandgap energy can also be defined by $E_g = \epsilon_{N+1} - \epsilon_N$, and the subband gap between the lowest and second lowest energy states in the conduction band is hereafter referred to as $\Delta_{sub} = \epsilon_{N+2} - \epsilon_{N+1}$.

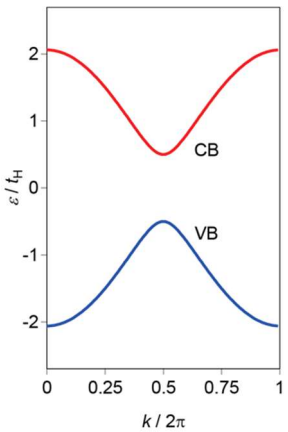

Fig. S6. Example of the band structure of a dimer chain model.

To describe the light-induced electron dynamics, we add a time-dependent external potential $\hat{V}_{ext}(t)$ to the unperturbed Hamiltonian $\hat{H}_0$,

$$\hat{H}(t) = \hat{H}_0 + \hat{V}_{ext}(t). \quad (S2.3)$$

We describe the external field using the dipole approximation, and the external potential is given by

$$\hat{V}_{ext}(t) = -E(t) \cdot \hat{D} \tag{S2.4}$$

where $E(t)$ is the applied electric field, and $\hat{D}$ is the dipole operator defined as

$$\hat{D} = -e\frac{a_L}{2}\sum_{j=1}^{2N+1} j\,\hat{c}_j^{\dagger}\hat{c}_j. \tag{S2.5}$$

Since we consider pulsed laser excitation, we employ the following form for the electric field in the range $-T_{\text{pulse}}/2<t<T_{\text{pulse}}/2$:

$$E(t) = E_0 \sin(\omega_0 t)\cos^4\left(\frac{\pi}{T_{pulse}}t\right), \tag{S2.6}$$

and we assume that the field is zero outside this range. Here, E_0 is the peak field strength, and ω_0 is the mean frequency.

The laser-induced electron dynamics are described by the time-dependent Schrödinger equation,

$$i\hbar\frac{d}{dt}|\Psi(t)\rangle = \hat{H}(t)|\Psi(t)\rangle. \tag{S2.7}$$

Note that we use the N-electron ground state as the initial condition, $|\Psi(t=-\infty)\rangle = |\Psi_{GS}\rangle$, where N spin-less electrons occupy the lowest N eigenstates of the Hamiltonian $\hat{H}_0$ in Eq. (S2.1).

By employing the time-dependent wavefunction $|\Psi(t)\rangle$, we can compute the field-induced dipole moment per cell:

$$D(t) = \frac{1}{N}\langle\Psi(t)|\hat{D}|\Psi(t)\rangle. \tag{S2.8}$$

Furthermore, the power spectrum of the emitted harmonics can be evaluated using the dipole moment according to

$$I_{HHG}(\omega) = \left|\omega^2\int_{-T_{pulse}/2}^{T_{pulse}/2} dt\;\; e^{i\omega t}D(t)\cos^4\left(\frac{\pi}{T_{pulse}}t\right)\right|^2. \tag{S2.9}$$

Here, we use the envelope function of the applied laser field as a window function for the Fourier transform.

B. QD diameter dependence of HHG

Here, we compute the power spectra of HHG of one-dimensional QDs with different diameters using the dimer chain model introduced in the previous section. The QD diameter is defined by $d_n = (2N+1)a_L/2$. We set t_H to 0.94 eV and Δ to 1.75 eV to obtain E_g=1.75 eV and $m^* = 0.101m_0$ in the bulk limit ($N \to \infty$). These values correspond to the bandgap energy and the reduced electron–hole mass of CdSe reported in the literature. Figure S8a shows the computed power spectra $I_{HHG}(\omega)$ for a field strength of $E_0 = 11$ MV/cm. The emission intensity increases with the QD size, and harmonic peaks are clearly observed in each spectrum.

Both the bandgap energy E_g and the subband gap Δ_{sub} increase due to confinement as the QD diameter becomes smaller. However, as shown below, the suppression of HHG that is observed as the QD diameter decreases, is not a result of the increase of E_g. To assess the effect of confinement, we first discuss the diameter dependence of E_g and that of Δ_{sub}. Extended Data Fig. 1a shows that E_g converges to the bulk value, 1.75 eV, in the limit of large diameters. Δ_{sub} converges to zero in the limit of large diameters, i.e. continuous bands are formed. In other words, once the diameter decreases, the states become discrete due to confinement. To clarify that the bandgap renormalization does not have a significant impact on HHG, we also computed the HHG power spectra in the case of a constant bandgap energy equal to 1.75 eV. The bandgap energy is artificially tuned to this value for each d_n by changing the energy difference Δ. Figure S7b shows the results. By comparing Figs. S7a and b, we find that the bandgap renormalization does not have a significant effect on the diameter dependence of the HHG power spectra.

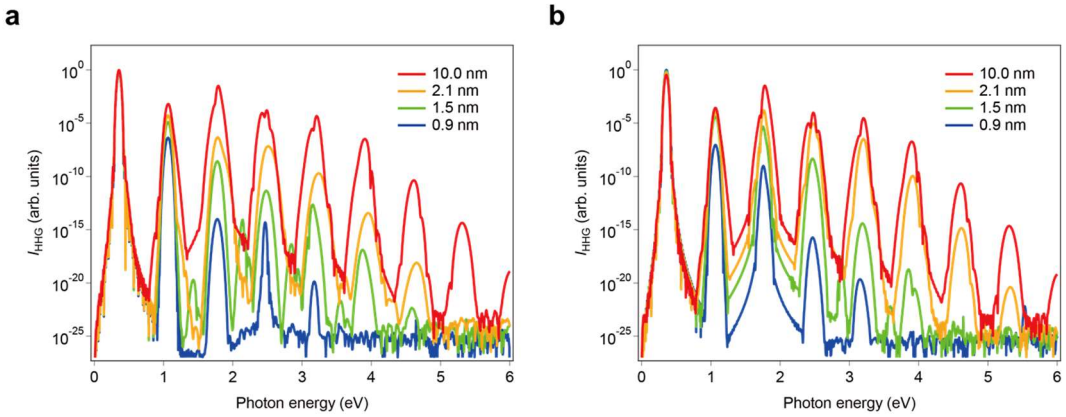

Fig. S7. HHG power spectra calculated using the dimer chain model for different QD diameters. **a,** The results for t_H = 0.94 eV and Δ = 1.75 eV. **b,** The results obtained by fixing the bandgap energy to 1.75 eV.

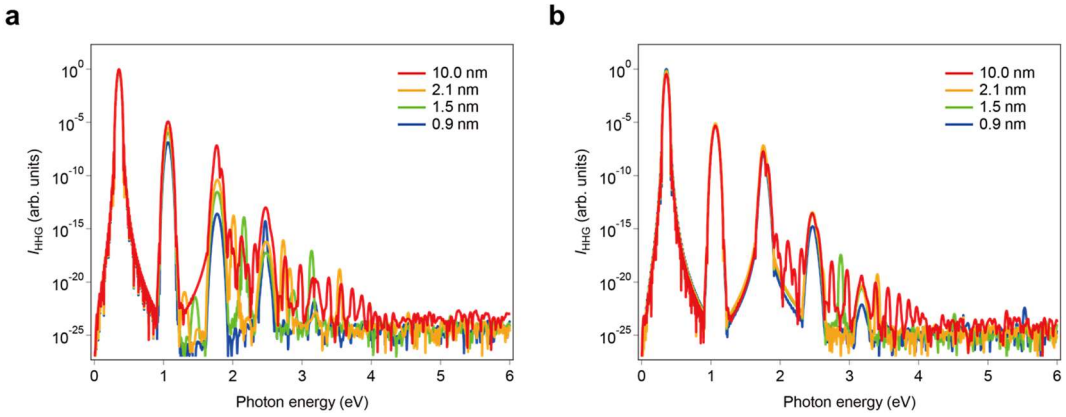

Fig. S8. The HHG power spectra calculated using a dimer chain model that employs the same parameters as those for Fig. S7 except for the intraband transition term, $\hat{V}_{ext}^{Intra}(t)$, which is set to zero. **a,** The results for a variable bandgap energy and **b,** those for a fixed bandgap energy.

C. Role of intraband transitions in photocarrier injection and HHG

Previous investigations have suggested that intraband transitions play an important role in HHG in solids [10]. Here, electron–hole pairs can be accelerated by external fields such as those of a laser, and the relative acceleration motion of electron–hole pairs in real-space corresponds to an intraband transition in the Brillouin zone. However, in small QDs, the real-space acceleration of electron–hole pairs is expected to be suppressed due to quantum confinement, and thus intraband transitions are also expected to be suppressed. Therefore, in this section, we discuss the suppression of HHG from the viewpoint of the intraband

transitions.

First, we define the intraband and interband transitions in the one-dimensional dimer chain model. As discussed above, the eigenstates of the Hamiltonian $\hat{H}_0$ can be categorized as either the N (lower energy) valence states or the $N+1$ (higher energy) conduction states. On the basis of this classification, we define intraband transitions as transitions between the same class of states, and interband transitions are transitions between the valence and conduction states. Therefore, we decompose the external potential into the intraband and interband transition terms as shown below:

$$\hat{V}_{ext}(t) = -E(t)\cdot\hat{D} = -E(t)\sum_{n=1}^{2N+1}\sum_{m=1}^{2N+1} D_{nm}\,\hat{a}_n^{\dagger}\hat{a}_m = \hat{V}_{ext}^{Intra}(t) + \hat{V}_{ext}^{Inter}(t), \qquad (S2.10)$$

where the intraband and interband transition terms are defined as

$$\hat{V}_{ext}^{Intra}(t) = -E(t)\left[\sum_{n=1}^{N}\sum_{m=1}^{N} D_{nm}\,\hat{a}_n^{\dagger}\hat{a}_m + \sum_{n=N+1}^{2N+1}\sum_{m=N+1}^{2N+1} D_{nm}\,\hat{a}_n^{\dagger}\hat{a}_m\right], \qquad (S2.11)$$

$$\hat{V}_{ext}^{Inter}(t) = -E(t)\left[\sum_{n=1}^{N}\sum_{m=N+1}^{2N+1} D_{nm}\,\hat{a}_n^{\dagger}\hat{a}_m + \sum_{n=1}^{N}\sum_{m=N+1}^{2N+1} D_{nm}\,\hat{a}_n^{\dagger}\hat{a}_m\right]. \qquad (S2.12)$$

Here, the intraband transition term $\hat{V}_{ext}^{Intra}(t)$ describes the transitions among the states with $1 \le n \le N$ and those among the states with $N+1 \le n \le 2N+1$. On the other hand, the interband transition term $\hat{V}_{ext}^{Inter}(t)$ describes only the transitions between valence and conduction states.

To investigate the role of the intraband transitions, we computed the HHG power spectra by setting $\hat{V}_{ext}^{Intra}(t) = 0$. Figure S8a shows the computed HHG power spectra in the case of $\hat{V}_{ext}^{Intra}(t) = 0$ for different QD diameters. Except for the intraband transition term $\hat{V}_{ext}^{Intra}(t)$, all calculation conditions are the same as those in the calculation for Fig. S8a. In addition, Figure S8b shows the spectra in the case of no intraband transition but with a fixed bandgap energy, which can be compared with the results shown in Fig. S7b.

Compared to Fig. S7a, the HHG power spectra in Fig. S8a show lower intensities. This confirms that the intraband transitions significantly enhance HHG [10]. Furthermore, the HHG power spectra in Fig. S8a also depend on the QD diameter; the HH peak intensities are suppressed when the QD diameter is reduced. On the other hand, as evidenced by Fig. S8b, the HH peak intensities are not significantly affected by the QD diameter when the bandgap energy is fixed. Hence, the reduction of HHG in Fig. S8a originates from the bandgap increase due to quantum confinement.

By comparing Figs. S7b and S8b, it can be confirmed that the significant reduction of the HHG in small QDs originates from the suppression of intraband transitions, because the HHG spectra are hardly reduced further once the intraband transitions are completely turned off. Furthermore, the HHG power spectra of small QDs in Fig. S7b are similar to the spectra in Fig. S8b. Therefore, the suppression of HHG by the reduction of the QD diameter can be explained by the suppression of intraband transitions due to the confinement effect.

In order to compare the calculation results with Fig. 2 in the main text, we evaluated the HH peak intensity of each harmonic order *h* according to the definition

$$I_h = \int_{\left(h-\frac{1}{2}\right)\omega_0}^{\left(h+\frac{1}{2}\right)\omega_0} d\omega\, I_{HHG}(\omega)\ , \qquad (S2.13)$$

and provide the detailed diameter dependence in Figs. S9a–c. We consider four calculation conditions: the full calculation close to the actual conditions where we assume t_H = 0.94 eV and Δ = 1.75 eV (red circles), the calculation with the artificially fixed bandgap energy (green squares), the calculation where we assume t_H = 0.94 eV and Δ = 1.75 eV but turn off the intraband transitions by assuming $\hat{V}_{ext}^{Intra}(t) = 0$ (purple triangles), and the calculation with an artificially fixed bandgap energy without intraband transitions (blue

upside-down triangles). As seen in these figures, the intensities of the 3rd, 5th, and 7th harmonics are significantly suppressed when we turn off the intraband transitions.

To elucidate the effect of the photocarrier injection, we also evaluate the number of conduction electrons n_{ex} after the laser irradiation using

$$n_{ex} = \sum_{n=N+1}^{2N+1} \langle \Psi(t)| \hat{a}_n^{\dagger} \hat{a}_n |\Psi(t)\rangle. \qquad (S2.14)$$

Figure S9d shows the conduction-state population after the laser irradiation as a function of the QD diameter. The results clearly depend on the calculation conditions: By comparing Fig. S9d and the other panels (a-c), we can confirm that the photocarrier injection and HHG show a similar behavior. This result indicates the quantum confinement in small QDs suppresses the intraband transitions, and then also the photocarrier injection process, which is the initial process in HHG processes, is suppressed.

To obtain further insights, we investigated how a change in the reduced electron–hole mass m^* affects the HH spectra. In this analysis, the reduced mass is tuned by manipulating the hopping parameter t_H. Figures S10a,b and Fig. 4c in the main text show the diameter dependence of I_3, I_5, and I_7, respectively, for three different masses. In these simulations, the bandgap energy was fixed to the bulk value, 1.75 eV. As can be seen in these figures, the HH intensity of smaller QDs deviates stronger from the bulk limit when the reduced masses m^* becomes smaller. This fact indicates that the confinement effect becomes stronger when the reduced mass becomes smaller. To assess the confinement effect, we investigated the relation between HHG and the subband gap energy Δ_{sub}. Figure 11a,b and Extended Data Fig. 1c show I_3, I_5, and I_7 as a function of Δ_{sub} for different reduced masses. The figures clarify that the HH intensities for different reduced masses start to deviate from the bulk response at similar Δ_{sub} values. Hence, the subband gap energy is expected to play an important role in the effect of quantum confinement on HHG.

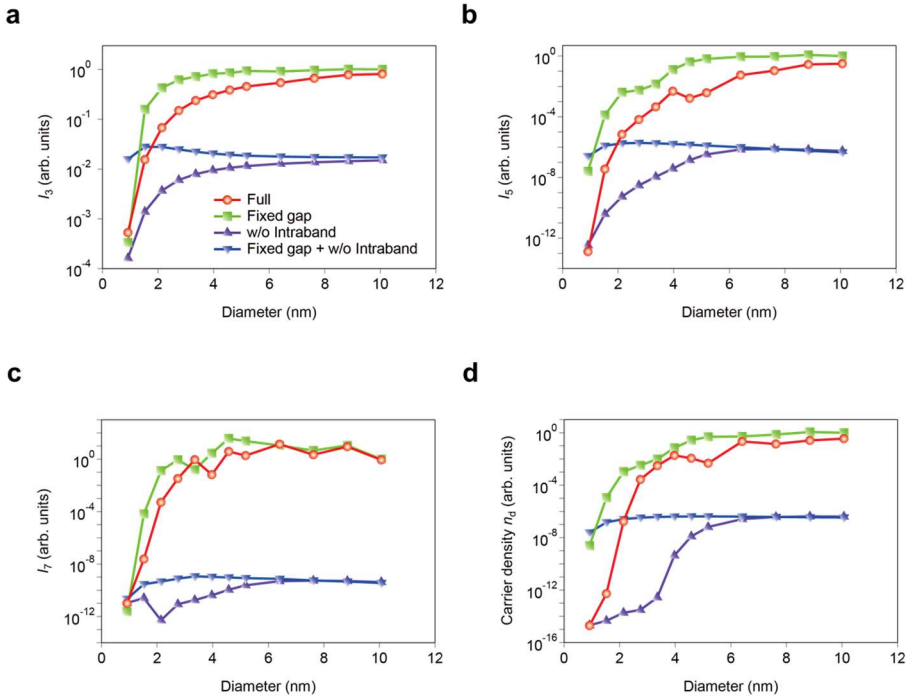

Fig. S9. The impact of the calculation conditions on the diameter dependence of HHG and the photocarrier injection. **a,** Diameter dependence of the 3rd harmonic, **b,** that of the 5th harmonic, and **c,** that of the 7th harmonic. The four calculation conditions are: the full calculation where we assume t_H = 0.94 eV and Δ = 1.75 eV, the fixed-gap calculation, the calculation without intraband transitions, and the fixed-gap calculation without intraband transitions. **d,** The number of excited electrons per cell as a function of the QD diameter.

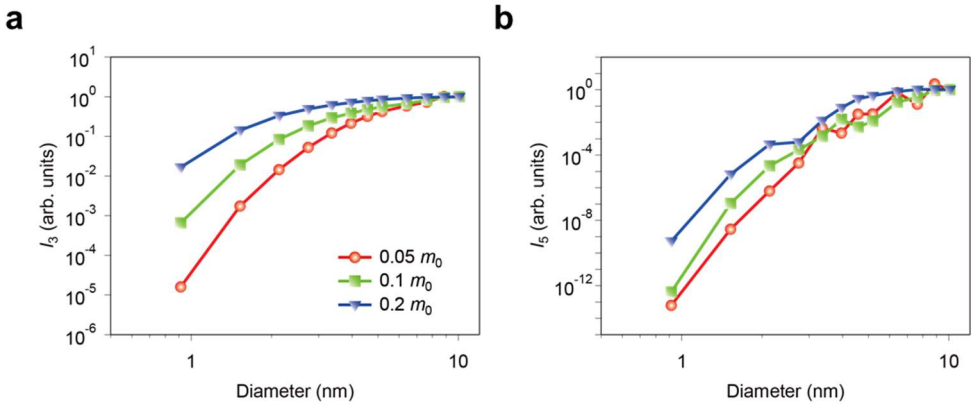

Fig. S10. Diameter dependence of **a,** the 3rd harmonic and **b,** 5th harmonic for different reduced electron–hole masses.

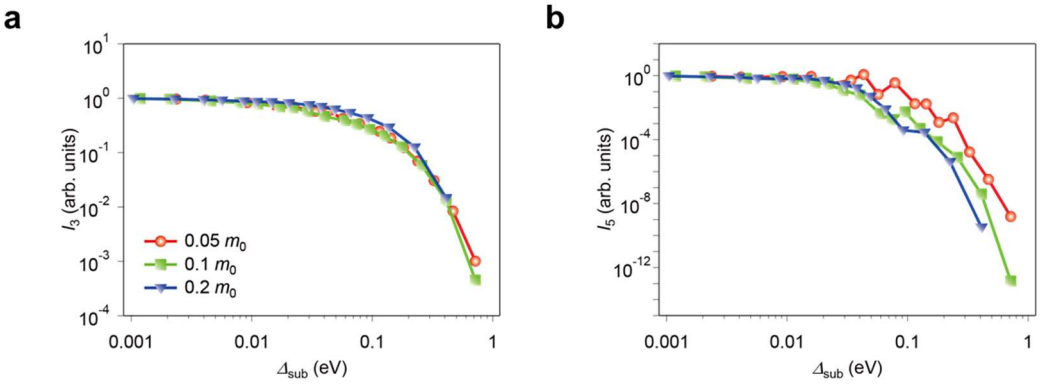

Fig. S11. Subband-gap energy dependence of **a,** the 3rd harmonic and **b,** the 5th harmonic for different reduced electron–hole masses.

D. Intraband and interband transitions from the viewpoint of perturbation analysis

To study the roles of intraband and interband transitions in the field-induced dynamics we use the time-dependent Schrödinger equation in the interaction picture,

$$i\hbar\frac{d}{dt}|\Psi_I(t)\rangle = \hat{V}^I{}_{ext}(t)|\Psi_I(t)\rangle, \qquad (S2.15)$$

where the wavefunction $|\Psi_I(t)\rangle$ and the potential $\hat{V}^I{}_{ext}(t)$ in the interaction picture are defined as follows:

$$|\Psi_I(t)\rangle = e^{i\hat{H}_0 t/\hbar}|\Psi(t)\rangle, \qquad (S2.16)$$

$$\hat{V}^I_{ext}(t) = e^{i\hat{H}_0 t/\hbar}\hat{V}_{ext}(t)e^{-i\hat{H}_0 t/\hbar}. \qquad (S2.17)$$

Then, we consider the perturbative expansion of the wavefunction $|\Psi_I(t)\rangle$ in powers of the interaction,

$$|\Psi_I(t)\rangle = \left|\Psi_I^{(0)}\right\rangle + \left|\Psi_I^{(1)}(t)\right\rangle + \left|\Psi_I^{(2)}(t)\right\rangle \cdots . \quad (S2.18)$$

By substituting Eq. $(S2.18)$ into Eq. $(S2.15)$, we obtain the following expression for the *n*th order wavefunction:

$$\left|\Psi_I^{(n)}(t)\right\rangle = \frac{1}{(i\hbar)^n}\int_0^t dt_1 \int_0^{t_1} dt_2 \cdots \int_0^{t_{n-1}} dt_n \, \hat{V}_{ext}^I(t_1)\hat{V}_{ext}^I(t_2)\cdots \hat{V}_{ext}^I(t_n)\left|\Psi_I^{(0)}\right\rangle. \quad (S2.19)$$

By decomposing the potential $\hat{V}_{ext}^I(t)$ into the components of the intraband and interband transitions, $\hat{V}_{ext}^{I,Intra}(t)$ and $\hat{V}_{ext}^{I,Inter}(t)$, respectively, the wavefunction in Eq. $(S2.19)$ can be rewritten as

$$\begin{aligned}\left|\Psi_I^{(n)}(t)\right\rangle = {} & \tfrac{1}{(i\hbar)^n}\textstyle\int_0^t dt_1 \int_0^{t_1} dt_2 \cdots \int_0^{t_{n-1}} dt_n \, \hat{V}_{ext}^{I,Inter}(t_1)\hat{V}_{ext}^{I,Inter}(t_2)\cdots \hat{V}_{ext}^{I,Inter}(t_n)\left|\Psi_I^{(0)}\right\rangle \\ & + \tfrac{1}{(i\hbar)^n}\textstyle\int_0^t dt_1 \int_0^{t_1} dt_2 \cdots \int_0^{t_{n-1}} dt_n \, \hat{V}_{ext}^{I,Intra}(t_1)\hat{V}_{ext}^{I,Inter}(t_2)\cdots \hat{V}_{ext}^{I,Inter}(t_n)\left|\Psi_I^{(0)}\right\rangle + \cdots \\ & + \frac{1}{(i\hbar)^n}\int_0^t dt_1 \int_0^{t_1} dt_2 \cdots \int_0^{t_{n-1}} dt_n \, \hat{V}_{ext}^{I,Intra}(t_1)\hat{V}_{ext}^{I,Intra}(t_2)\cdots \hat{V}_{ext}^{I,Intra}(t_n)\left|\Psi_I^{(0)}\right\rangle. \quad (S2.20)\end{aligned}$$

Here, only the first term on the right-hand side contains no intraband-transition component. Hence, all other terms vanish if $\hat{V}_{ext}^{I,Intra}(t)$ is set to zero. In other words, the contributions of these other terms increase when the intraband transitions are enhanced as schematically described in Fig. 4d and Extended Data Fig. 2 in the main text, where these additional VB–CB excitation channels dominate HHG in larger QDs.

References

1. Kim, S. et al. Phase segregated $Cu_{2-x}Se/Ni_3Se_4$ bimetallic selenide nanocrystals formed through the cation exchange reaction for active water oxidation precatalysts. *Chem. Sci.* **11**, 1523–1530 (2020).
2. Fenton, J. L., Steimle, B. C. & Schaak, R. E. Tunable intraparticle frameworks for creating complex heterostructured nanoparticle libraries. *Science* **360**, 513–517 (2018).
3. Li, J., Chen, J., Shen, Y. & Peng, X. Extinction coefficient per CdE (E = Se or S) unit for zinc-blende CdE nanocrystals. *Nano Res.* **11**, 3991–4004 (2018).
4. Li, J. J. et al. Large-scale synthesis of nearly monodisperse CdSe/CdS core/shell nanocrystals using air-stable reagents via successive ion layer adsorption and reaction. *J. Am. Chem. Soc.* **125**, 12567–12575 (2003).
5. Yu, W. W. & Peng, X. G. Formation of high-quality CdS and other II-VI semiconductor nanocrystals in noncoordinating solvents: Tunable reactivity of monomers. *Angew. Chem. Int. Ed.* **41**, 2368–2371 (2002).
6. Keldysh, L. Ionization in the field of a strong electromagnetic wave. Sov. Phys. JETP **20**, 1307–1314 (1965).
7. Sanari, Y et al. Generation of wavelength-tunable few-cycle pulses in the mid-infrared at repetition rates up to 10 kHz. *Opt. Lett.* **46**, 5280–5283 (2021).
8. Klimov, V. I., McGuire, J. A., Schaller, R. D. & Rupasov, V. I. Scaling of multiexciton lifetimes in semiconductor nanocrystals. *Phys. Rev. B* **77**, 195324 (2008).
9. Tahara, H., Sakamoto, M., Teranishi, T. & Kanemitsu, Y. Quantum coherence of multiple excitons governs absorption cross-sections of PbS/CdS core/shell nanocrystals. *Nat. Commun.* **9**, 3179 (2018).
10. Golde, D., Meier, T. & Koch, S.W. High harmonics generated in semiconductor nanostructures by the coupled dynamics of optical inter- and intraband excitations. *Phys. Rev. B* **77**, 075330 (2008).